Biosensors and Bioelectronics 165 (2020) 112346

Contents lists available at ScienceDirect

Biosensors and Bioelectronics

journal homepage: http://www.elsevier.com/locate/bios

L-phenylalanine-imprinted polydopamine-coated CdS/CdSe n-n type II heterojunction as an ultrasensitive photoelectrochemical biosensor for the PKU monitoring

Kheibar Dashtian [a], Shaaker Hajati [b,*], Mehrorang Ghaedi [a,**]

[a] Chemistry Department, Yasouj University, Yasouj, 75918-74831, Iran
[b] Department of Semiconductors, Materials and Energy Research Center (MERC), P.O. Box 31787-316, Tehran, Iran

ARTICLE INFO

Keywords:
L-phenylalanine
Heterojunction
Photoelectrochemical biosensor
Molecular imprinted polydopamine
Zn marigold flower

ABSTRACT

A simple and highly sensitive photoelectrochemical biosensor towards L-phenylalanine, as a kind of typical essential amino acid and phenylketonuria biomarker was developed on a surface molecular imprinted (MIP) polydopamine-coated CdS/CdSe/Zn heterojunction. Hierarchical marigold flower-like Zn layer decorated by n-type dichalcogenides interfacial heterojunction was successfully designed and synthesized on Ti foil for PEC converter by in situ electrodeposition. A visible-light-driven molecular imprinting film was prepared through the electropolymerization of dopamine in the presence of L-Phe as biomarker. The combination of bio-MIP and photoelectrochemistry overcomes the defects of the PEC method, which is the absence of selectivity, and offers a new PEC sensor with high sensitivity and selectivity based on visible-light-driven heterojunction and biopolymer-enhanced strategy. The unique interfacial between the Zn marigold flower layer as low work function support and CdS/CdSe n-n heterojunction as well as n-type characteristics of polydopamine imprinted by L-Phe biomarker drastically increase the light trapping and absorption in the visible range, and dramatically inhibit the charge carrier recombination, which is crucial for boosting the Bio-PEC activity. Photocatalytic, electrocatalytic and physicochemical properties of the above-mentioned layers were fully characterized. As-prepared PEC biosensor displayed superb performance for the detection of L-Phe biomarker in the optimized condition obtained from central composite design modeling, showing two linear range 0.005–2.5 and 2.5–130 μM and a low detection limit of 0.9 nM. This work suggests that such L-Phe-imprinted polydopamine-coated Zn/CdS/CdSe heterojunction is greatly promising for being applied in photoelectrochemical biosensing with high photo-electron conversion efficiency.

1. Introduction

Phenylketonuria (PKU) is a widespread disease in the intrinsic disorder of amino acid metabolism, which often emerges in children and youngsters (Banik et al., 2016; MacDonald et al., 2004). PKU can harm the neonatal nervous system, so untreated PKU can often lead to severe mental retardation as well as physical and behavioral abnormalities such as heart problems (Khemir et al., 2011), small head (Hasanzadeh et al., 2018), and low birth weight. Moreover, it causes epilepsy and eventually leads to death (Campistol and Plecko, 2015). Although PKU is not curable, the early identification and effective treatment of PKU could prevent irreparable damage (Xu et al., 2019b). Most patients are diagnosed via newborn screening, in which non-invasive blood or urine sampling is more appropriate because of their convenience and harmlessness for newborns (Szabo' et al., 2015; Yan et al., 2020). Moreover, the reliable point-of-care testing of the biomarkers may expedite the diagnosis and management of the underlying medical conditions (Christodouleas et al., 2018; Min et al., 2018). The detection of PKU markers in body fluid has been done with bacterial inhibition assay (Isabella et al., 2018), immunoassays using fluorescence (Long, 2013) and electrochemical methods under the assistance of an aptamer or DNA using high-performance liquid chromatography or gas chromatography−mass spectrometry (Aghaei et al., 2017; Idili et al., 2019; Naghib et al., 2012). Since these methods usually require a long time for sample

* Corresponding author. Tel.: +98 74 33223048; fax: +98 74 33223048.
** Corresponding author.
E-mail addresses: Kdasht68@gmail.com (K. Dashtian), shajati49@gmail.com, hajati@mail.yu.ac.ir (S. Hajati), m_ghaedi@mail.yu.ac.ir (M. Ghaedi).

https://doi.org/10.1016/j.bios.2020.112346
Received 6 March 2020; Received in revised form 26 May 2020; Accepted 31 May 2020
Available online 5 June 2020

processing, modern system based on developed electrochemical analysis, with the advantages of rapid response, high sensitivity, and simple handling can be used for the development of next-generation clinical diagnostic technology (Moreira et al., 2018; Xu et al., 2019b). Because PKU is a disease caused by the deficiency of the metabolic phenylalanine hydroxylase (PAH) enzyme, PAH activity measurements has been proposed as a method of PKU diagnosis (Heintz et al., 2012), while complicated handling procedures and the requirement for special care with enzymatic activity make these methods less robust and difficult for continuous in situ analysis (Charkhabi et al., 2018; Sassolas et al., 2012; Wick et al., 2019). Accordingly, PKU treatment demands urgent innovative interventions, developing a method based on direct detection of L-Phe as the most effective PKU marker without the employment of bio-recognizers, which is the most appropriate pathway to overcome the above-mentioned limitations and thus suitably μM analysis of L-Phe (Cheung et al., 2019; Idili et al., 2019; Zhou et al., 2018). This paper addresses the critical need for novel reliable tools for the predictive, label-free and minimally invasive early detection of PKU processes. It will bring a novel, rapid, sensitive, selective and efficient lab-on-chip tool employing the electrochemical deposition to address new frontiers in detection, early diagnosis and monitoring of PKU disorder (Chałupniak and Merkoç;i 2017; Tiwari et al., 2016; Wongkaew et al., 2018; Xu et al., 2019a). This new modern device is a versatile handheld platform based on photo-electrochemical, which opens an innovative gate to develop monitoring of many other key biomarkers (Cao et al., 2020; Lv et al., 2018; Qiu et al., 2018) as well as aims to make a transformative impact on the life of newborn patients affected by PKU (Hong et al., 2018). To beat this challenge, we designed push state-of-the-art technology towards an unprecedented sensor construct making the most of biological, chemical, physical, analytical, electronic, magnetic and engineering means (Ibrahim et al., 2018; Shi et al., 2019b). We have reasoned that proposed assay as a new and promising analytical, bioanalytical and physical multiple technique (Zhao et al., 2017). It is based on coupling PEC active species and selective organic biopolymer and inorganic photo-absorbent semiconducting materials to improve charge transport properties under light illumination with low background signals (Fan et al., 2019; Wang et al., 2017b; Yu et al., 2019). The electron transfers among analyte, photoactive species and electrode under photo-irradiation, which could be an effective diagnosis and detection modality that is easily applicable to clinical settings (Song et al., 2018). This assay benefits from a photoactive molecularly imprinted biopolymer, for overcoming poor selectivity and sensitivity of conventional sensing systems due to the selective interaction between biopolymer and L-Phe analyte (Tsafack et al., 2000; Wang et al., 2017a; Yang et al., 2019). Generally, the molecular imprinting (MI) technique provides a mimetic receptor system to recognize the target molecule (Kolaei et al., 2016; Shi et al., 2019a). In addition, due to the coupling of the proposed material species, a novel selective type II heterojunction structure will be formed on low work function metallic nanoparticles-coated titanium foil as opal electrode. This is expected to show better PEC performance due to highly efficient light trapping, improved charge separation and charge collection (Lee et al., 2016; Mao et al., 2019; Yang et al., 2018).

2. Experimental method

2.1. Materials

$CdSO_4$, $NaCH_3COOH$, $Na_2S_2O_3$, $Na_2Se_2O_3$, $Zn(CH_3COOH)_2.2H_2O$, Na_2S, teriethanol amine (TEA), ethylenediaminetetraacetic acid (EDTA), Tween 80, L-phenylalanine (L-Phe), ethylene glycol (EG), ascorbic acid (AA), dopamine (DA), HCl, NaOH, Tris-HCl buffer, melamine, L-tyrosine, thymine, L-cysteine, guanine, adenine, citric acid, adipic acid, bovine serum albumin, acetone and ethanol were obtained from Merck (Darmstadt, Germany). As received materials were used without any further purification. Phosphate buffered saline (PBS) pellet and 0.3 mm thick Ti foil (99.7%) were acquired from Sigma-Aldrich. Stock solutions (1.0 mmol L^{-1}) were prepared by dissolving the standard powder in DI water followed by its dilution with a nitrogen-assisted deaerated buffer supporting electrolyte (0.1 mol L^{-1} PBS containing 1.0 mM AA (pH 7.0)) to achieve the desired concentration of solutions required for running experiments.

2.2. Electrodeposition of Zn marigold flower layer on Ti foil

Before the electrodeposition of the Zn marigold flower as low work function layer on Ti foil (Zn/Ti), a Ti foil (1 cm × 3 cm) was wet-polished followed by the removal of titania residue by sonicating in acetone, ethanol and distilled water for 10 min. Deposition solution was a mixture of sodium acetate (0.5 M) as a complexing and capping agent, zinc acetate (0.75 M) and 100 mL of anhydrous ethylene glycol. The electroplating of the Zn marigold flower layer was performed in the prepared deposition solution at 70 °C by CA with 1.0 V potential for 500 s. After the deposition, to remove any remaining sodium acetate and other unreacted reagents, the electrode was immersed and rinsed in distilled water (70 °C) for 3 times and finally dried at ambient temperature.

2.3. Electrodeposition of double-shelled CdS- and CdSe-Cosensitized Zn/Ti substrate

The CdS thin film was coated on Zn/Ti (CdS–Zn/Ti) in an electrolytic bath containing 0.07 M $CdSO_4$, 0.7 M $Na_2S_2O_3$, and 0.1 M EDTA in the volumetric ratio of 1:4:3 (the solution pH was maintained at ~4). A three-electrode configuration was used for the deposition of CdS on Zn/Ti substrate as working electrode at 50 °C for 450 s in constant potential of −0.85 V. After the deposition, to remove any remaining reagents, the electrode was immersed and rinsed in distilled water (70 °C) for 3 times and finally dried at ambient temperature. Subsequently, an aqueous solution composed of 0.02 M $Cd(OAc)_2$, 0.07 M Na_2SeO_3, and 0.04 M EDTA was used as electrolyte for the electrodeposition of CdSe on the CdS–Zn/Ti substrate at the potential of −1.5 V for 450 s. Finally, to remove any remaining reagents, the CdSe–CdS–Zn/Ti electrode was immersed and rinsed in distilled water followed by drying at ambient temperature.

2.4. Electrodeposition of L-Phe-imprinted polydopamine on CdSe–CdS–Zn/Ti

The L-Phe-imprinted polydopamine (L-Phe-IPDA) as photoactive selective layer coated on CdSe–CdS–Zn/Ti substrate (L-Phe-IPDA-CdS-CdSe-Zn/Ti) was fabricated by cyclic voltammetry method for dopamine polymerization in the presence of L-Phe biomarker target as follows: 15 mg/mL dopamine-HCl was prepared in degassed double distilled water followed by adding and dissolving appropriate amounts of Tris buffer solution (TBS, pH 7.4, 130 mg/mL containing 0.03% Tween 80), L-Phe (7.5 mg/mL), KCl (10 mg/mL) and NaCl (300 mg/mL) by magnetic stirring and nitrogen bubbling for 1.0 h. The solution was then poured in electrochemical cell including Pt counter electrode, Ag/AgCl reference electrode and CdS–CdSe–Zn/Ti as photoactive substrate. The voltage and scanning rate for the electrochemical reduction of dopamine-containing L-Phe onto the CdS–CdSe–Zn/Ti substrate were set to be within the range of 1.5 V to −1.5 V and at 50 mV/s, respectively. After each cycle, a decrease in the area enclosed with the voltammogram curve was observed due to the imprinting of L-Phe-containing polydopamine on the CdS–CdSe–Zn/Ti substrate. After 20 cycles, the amount of deposited L-Phe-IPDA led to nearly full insulation of the CdS–CdSe–Zn/Ti substrate. For comparisons, non-imprinting polydopamine (NIPDA) was prepared similar to the above-mentioned method in the absence of L-Phe target. All steps for L-Phe-IPDA and L-Phe-IPDA-CdS-CdSe-Zn/Ti preparation were schematically illustrated in Schemes 1 and 2, respectively.

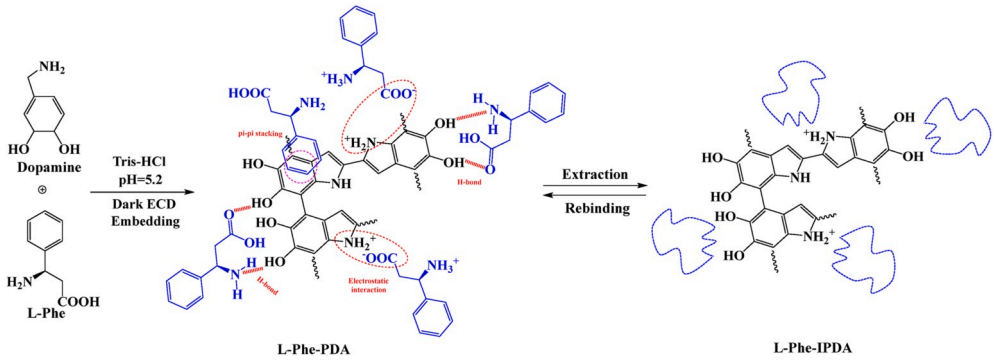

Scheme 1. The schematic diagram of the preparation of the L-Phe-IPDA.

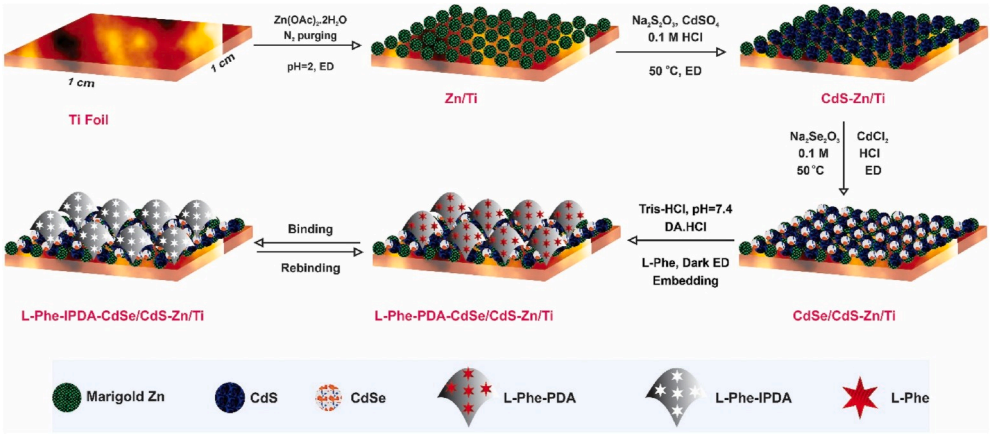

Scheme 2. The schematic diagram of the preparation of the L-Phe-IPDA-CdS-CdSe-Zn/Ti.

2.5. Samples characterization

A Metrohm 691 pH meter (Switzerland) was applied to measure the desired pH of the working solution, which was set using dilute NaOH or HCl. An electron beam of energy 15.00 keV was applied in field emission scanning electron microscopy (FESEM: Sigma, Zeiss, Jena, Germany) to observe the morphology of constituents of the working electrode. The FESEM equipped with energy-dispersive X-ray spectrometry (EDX) with solid-state detector (Oxford INCA II) was applied to acquire the EDX spectrum of the sample to obtain its elemental composition. The structure and phase of the components of working electrode were investigated using X-ray diffraction (XRD, PW, 1880; Philips, Amsterdam, Netherland) over 2θ range of 10.0–80.0° by CuKα radiation taken at 40 kV and 40 mA. The films were studied by UV–vis diffuse reflectance spectroscopy (UV–Vis DRS, Shimadzu UV-2550) to determine their optical characteristics. Other materials, apparatus, and software were applied based on manufacturer instructions as mentioned in our previously published works (Dashtian et al., 2019).

2.6. Electrochemical measurements

The photocurrent was tested with the commonly used three-electrode system, in which the platinum wire and Ag/AgCl electrode were used as the counter and reference electrodes, respectively. 0.1 M PBS was used as the electrolyte for all photoelectrochemical measurements. The prepared L-Phe-IPDA-CdS-CdSe-Zn/Ti was used as working electrode. In all tests, the light source was set to be blue, green, orange, red and violet LED lamp which was manually turned on for 10 s and subsequently turned off for 10 s in different cycles. To remove dissolved oxygen, highly pure nitrogen was bubbled into the electrolyte for 10 min and then the photocurrent was recorded with continuously flowing nitrogen. Electrochemical impedance spectroscopy (EIS), chronopotentiometry, cyclic voltammetry, Mott-Schottky, Bode-phase, and chronoamperometry were performed on an AutoLab PGSTAT at room temperature with 0.1 M KCl serving as supporting electrolyte.

2.7. Detection of L-Phe in real samples

The photoelectrochemical response of L-Phe-containing juice samples (apple and grape juice) was performed through the following steps: 1.0 g of samples, purchased from a local supermarket, was grounded and mixed with 0.1 mol L^{-1} HCl solution. After integrating for 15 min, the mixture was centrifuged for 15 min at 5000 rpm, and the supernatant was filtered through a 0.45 mm Whatman filter and diluted up to 10 mL with distilled water. The urine sample was obtained from a 4-year-old boy. For all samples, known amounts of L-Phe were added to 0.1 mol L^{-1} KCl solution containing 50.0 mL of the urine.

2.8. Experimental design

Small central composite design was applied to investigate the effects of the three operational factors on the photoelectrochemical response in presence of L-Phe analyte. The solution pH, light source wavelength and applied potential as studied parameters were selected based on the preliminary experiments. The design matrix and parameter levels are shown in Table S1. After running 15 trials, a second order polynomial model, analysis of variance and summary statistics were used for predicting the optimal point as well as main effect and interaction of parameters (Jafari et al., 2017; Tabatabaei et al., 2018).

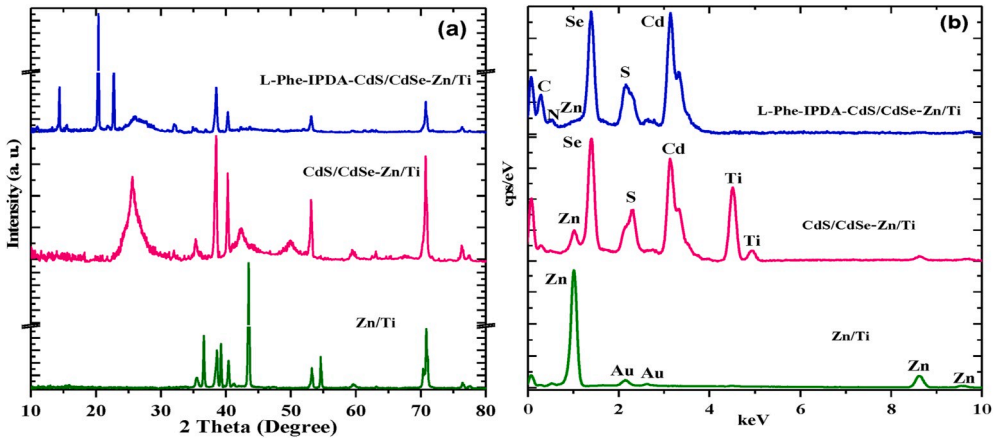

Fig. 1. XRD pattern (a) and EDS spectra (b) of as-prepared samples.

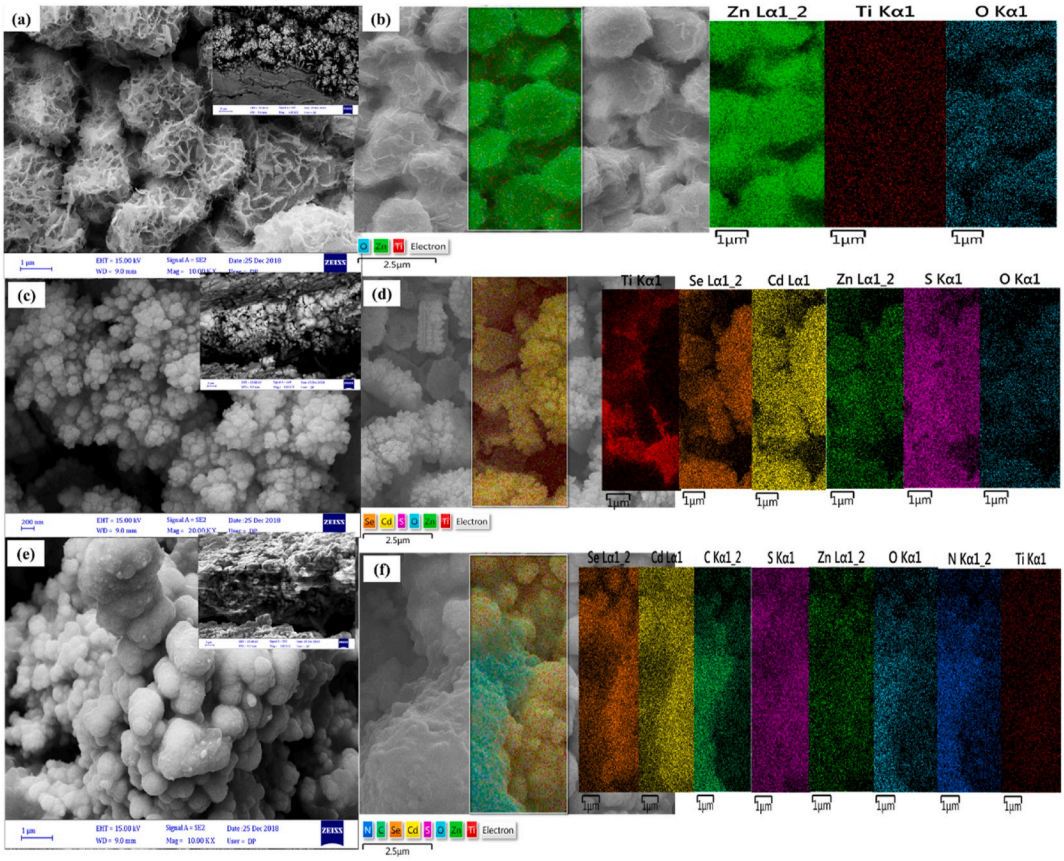

Fig. 2. FESEM images (a) and EDS mapping (b) of Zn marigold flower-like nanostructured thin-layer on Ti foil (up right inset of 2a is the cross-sectional view FESEM image), FESEM images (c) and EDS mapping (d) of spherically structured CdS/CdSe layer on Zn/Ti substrate (up right inset of 2c is the cross-sectional view FESEM image) and FESEM images (e) and EDS mapping (f) of as-prepared L-Phe-IPDA-CdS/CdSe–Zn/Ti (up right inset of 2e is the cross-sectional view FESEM image).

3. Results and discussions

3.1. Sample characterization

XRD pattern of Zn marigold flower-like nanostructured thin-film grown on Ti foil substrate showed sharp peaks at 2θ of 36.36, 39.08, 43.32, 54.47, 70.24 and 70.80°, which revealed that they were correlated with the 002, 010, 011, 012, 013 and 110 crystal planes, respectively in hexagonal structure (Reference: 2436-901-96) (Fig. 1a) (Shou et al., 2017). After CdS/CdSe deposition, there are some peaks at 25.5, 44.0, and 52.1° associated with the 111, 220, and 311 planes, which correspond to the cubic structure of cadmium sulfide (JCPDS No. 80–0019) and cadmium selenide nanocrystals (JCPDS No. 08–0459), respectively (Bang et al., 2012; Cao et al., 2013; Xu, 2019). After electrochemical deposition of the L-Phe-imprinted PDA on the CdS/CdS–Zn/Ti substrate, all of the above-mentioned peaks have appeared, while the addition of new sharp peaks at 2θ of 15.1, 20.1 and 21.5° may be due to the complex formation between the cadmium in the substrate and polydopamine. Polydopamine is able to form complexes with some metal atoms such as cadmium because of its free electron nitrogen atoms and the soft structure of this molecule. Thus, the new appeared peaks indicated to confirm the two-dimensional complex

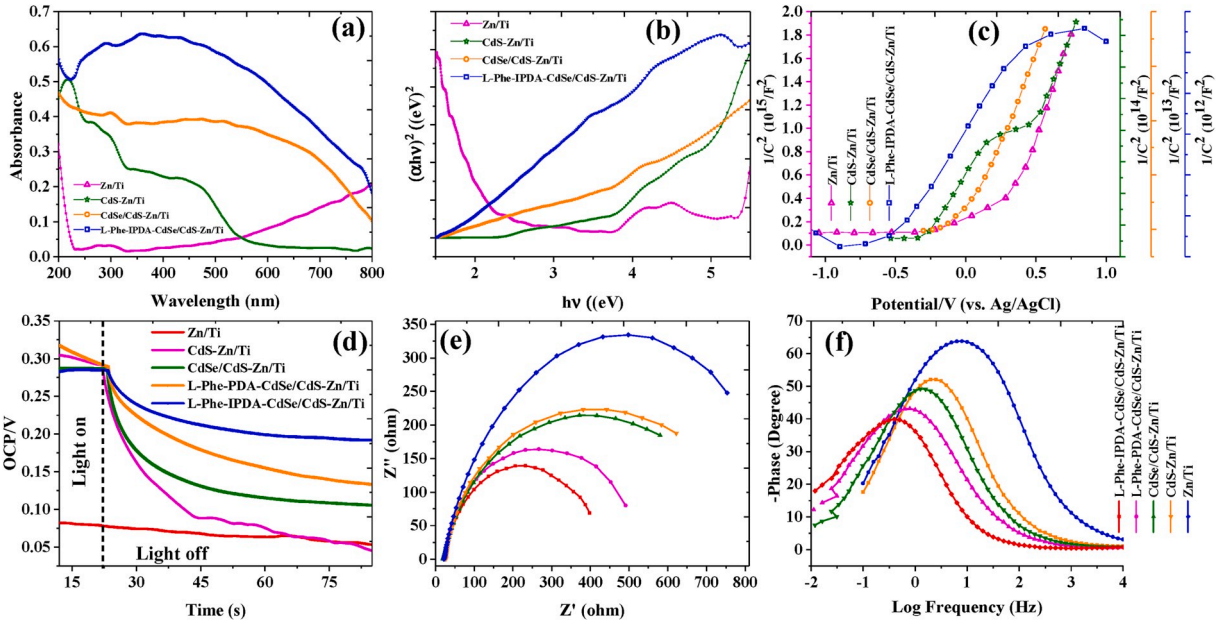

Fig. 3. UV–Vis DRS spectra (a), Tauc plot (b), Mott-Schottky plot (c), open-circuit potential diagram (d), EIS (e) and bod phase (f) of the as-prepared photoelectrodes.

formation between polydopamine and cadmium (Fig. 1a). The EDS spectrum of the Zn/Ti, CdS/CdSe–Zn/Ti and L-Phe-IPDA-CdS/CdSe–Zn/Ti have been presented in Fig. 1b, which indicates all of the proposed elements confirming that the experimental values were near to the theoretical values as calculated from EDS spectra.

The morphology of as-prepared electrodes was investigated using FE-SEM analysis. Fig. 2a shows the growth of marigold flower-like Zn nanostructured thin layer on the Ti foil surface. This highly ordered structure of high porosity makes it suitable for the growth of other layers. Cross-sectional FESEM image in upright inset in Fig. 2a showed a thickness of about 1.0 μm for the Zn marigold flower-like layer. The uniform distribution of the presence of elements was investigated by the EDS mapping and the results confirmed the uniform dispersion of Zn on the Ti substrate. Apparently, the appeared oxygen is related to the surface adsorbed oxygen (Fig. 2b).

Spherical CdS/CdSe nanoparticles with an average size of about 40 nm in uniform distribution (elemental mapping of Cd, Se, and S in the netlike CdSe and CdS) have been well grown on the Zn/Ti surface (Fig. 2c and d). Cross-sectional FESEM image in the bottom right inset in Fig. 2c showed a thickness of about 2.0 μm for the CdS/CdSe layer. The results provide the efficiency of the electrochemical stabilization method as an efficient option for growing uniform nanostructured layers and achieving mass production of these layers. FE-SEM images of L-Phe-imprinted PDA layer on the CdS/CdSe–Zn/Ti electrode showed spherical, smooth and compact L-Phe-PDA nanoparticles (Fig. 2e and f). The thin L-Phe-imprinted PDA layer was good for charge transport and the surface imprinted sites accelerate the speed of specific recognition of L-Phe target, which effectively enhances the sensing performance. Cross-sectional FESEM image in the upright inset in Fig. 2e showed a thickness of about 1.0 μm for the L-Phe-imprinted PDA layer. Generally, for applications in various PEC systems, such a unique morphology can expose more active sites, accommodate more target molecule as well as facilitate the connection between the internal active material and electrolyte. The uniform distribution of the Ti, Se, Cd, S, Zn, O, Zn and N elements in the mentioned electrode was also successfully confirmed by the EDS mapping method (Fig. 2f).

The light-harvesting capacity of the samples was demonstrated by their UV–Vis diffuse reflectance spectra (DRS) in Fig. 3a. Zn/Ti shows no obvious absorption edge in the range from 200 to 800 nm, which is due to its metallic property. The absorption edges of CdS and CdSe are located at 550 and 800 nm exhibiting their excellent visible light absorption capacity. Furthermore, it is seen that the light absorption capacity of the CdS/CdSe–Zn/Ti after coating the L-Phe-IPDA is superior to others, which is due to the good polymerization and π-plane conjugation degree of PDA. In addition, L-Phe-imprinted PDA resembles either electronic-ionic hybrid conductor due to its π-system and act as an effective photosensitizer and electrons donor to improve the separation of electrons-holes. The band gap of each sample was calculated using the Kubelka-Munk function (Fig. 3b). The position of conductive band (CB) and valence band (VB) was estimated according to the transformed Tauc plots and empirical formula where confirmed by mott Schottky analysis (Dashtian et al. 2018, 2019).

The Mott-Schottky curves of Zn/Ti, CdS–Zn/Ti, CdS/CdSe–Zn/Ti and L-Phe-IPDA-CdS/CdSe–Zn/Ti in 0.5 mol L^{-1} Na_2SO_4 solution were measured in a standard three-electrode electrochemical cell. The three-electrode system consists of Pt film, Ti-based (coated with 1 cm^2 of Zn/Ti, CdS–Zn/Ti, CdS/CdSe–Zn/Ti and L-Phe-IPDA-CdS/CdSe–Zn/Ti films), and Ag/AgCl electrode. The applied voltage to the Ti working electrode for photocurrent was 0 V, and the applied potential for Mott-Schottky curves varied from −0.1 V to 0.1 V, and the frequency scan was 10 kHz. Besides, for comparison, the Mott-Schottky of each pure sample was conducted. The flat band potential (E_{FB}) of pure CdS, pure CdSe and pure L-Phe-IPDA can be obtained using Mott-Schottky analysis by extending the linear section to $1/C^2 = 0$ (See Fig. 3c) according to our previous report (Dashtian et al., 2019). The E_{FB} values of pure CdSe, pure CdS and pure L-Phe-IPDA were obtained to be −0.35, −0.15 and 0.00 V, respectively, vs NHE. In addition, the positive slope of the linear part indicates that all samples exhibit n-type semiconductor properties. The E_{CB} values are approximately equal to E_{FB} for these n-type semiconductors, and the relevant parameters are summarized in Table S2.

The recombination-separation behavior of the photogenerated electron-holes was studied by the photo-chronopotentiometry using the open-circuit potential (OCP) diagram (Fig. 3d) after electron excitation under blue light radiation source. The magnitude of the potential and the rate of decay of the OCP were investigated and the results showed that the slope of the OCP decay for the L-Phe-IPDA-CdS/CdSe–Zn/Ti electrode was slower than that of the other electrodes. It can also be said that after each electrochemical deposition step, the rate of charge carriers decay was decreased and their lifetime increased. This indicates successful bands alignment of L-Phe-IPDA, CdS and CdSe photoactive

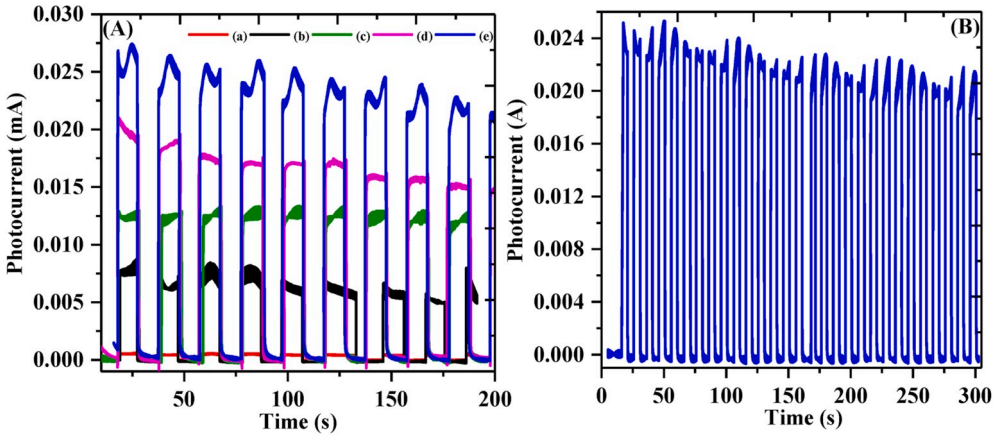

Fig. 4. (A) Photocurrent responses of Zn/Ti (a), CdS–Zn/Ti (b), CdS/CdSe–Zn/Ti (c), L-Phe-PDA-CdS/CdSe–Zn/Ti (d) and L-Phe-IPDA-CdS/CdSe–Zn/Ti (e) and (B) photocurrent stability of L-Phe-IPDA-CdS/CdSe–Zn/Ti in 0.1 M PBS at 0.6 V applied potential under visible light irradiation.

semiconductors and increases the surface area of each step compared to the previous step (Fig. 3d). Prior to the extraction of L-Phe species from PDA, the rate of OCP was higher than its rate of decline after L-Phe extraction, which indicates that the L-Phe acts as a space hindrance layer to prevent electron-hole transferring.

To better understand the promotion of PEC process, we further used photoelectrochemical impedance spectra (EIS) to analyze the charge transfers in the as-prepared PEC sensor (Fig. 3e). EIS consists of two parts; the semicircle diameter, which is detected at higher frequencies, presents the limited process for charge-transfer resistance (Rct) and the linear part, which is obtained at lower frequencies, symbolizes the diffusion-limited process. The Zn/Ti electrode reveals a relatively high Rct value, which is significantly decreased by CdS and CdSe deposition, that causes the separation of photoinduced electron-hole pairs and makes the rapid charge transfer from the surface of CdS/CdSe to the surface of Zn/Ti. After further modification of L-Phe-PDA, the Rct decreased obviously, which is due to the well aligned band structure between CdS/CdSe and L-Phe-PDA. The Rct value marginally decreases after L-Phe extraction from PDA polymer because of good conductivities and π-conjugation of PDA. The Bode plot of the Zn/Ti shows a peak at high frequency region, suggesting that at least a charge transfer process exists during the PEC, which is attributed to the charging of space charge layer (Fig. 3f). Other layer deposition leads to decreased and shifted peak toward lower frequency, indicating a decreased space charge layer and improved surface reaction process. In addition, the electron lifetime in prepared electrodes was correlated with the frequency peaks in Bode phase plots (Fig. 3f) according to our previous report (Dashtian et al. 2018, 2019). There is almost change after each layer deposition due to the decrease in space charge layer (depletion layer) demonstrating that the Zn as low work function agent as well as CdS and CdSe as photo-active agent can prolong the lifetime in samples. However, the L-Phe-IPDA-CdS/CdSe–Zn/Ti possesses a longer electron lifetime when compared with the other, identifying that the heterojunction of IPDA, CdS and CdSe layers can prolong the electron lifetime and facilitate charge transport.

Photoelectric behaviors of Zn/Ti, CdS–Zn/Ti, CdS/CdSe–Zn/Ti, L-Phe-PDA-CdS/CdSe–Zn/Ti and L-Phe-IPDA-CdS/CdSe–Zn/Ti were examined by recording the photocurrent response of each electrode in PBS solution (Fig. 4A). The photocurrents of L-Phe-PDA-CdS/CdSe–Zn/Ti and L-Phe-IPDA-CdS/CdSe–Zn/Ti electrodes were observed to be much higher than that of others, indicating that the PDA nanoparticles could greatly enhance the photoelectric response of Zn–CdS/CdSe due to well π-plane conjugation. While photocurrent intensity before the L-Phe extraction from PDA structure was lower than that after the L-Phe extraction which is due to the hindrance effect of L-Phe. The L-Phe-IPDA-CdS/CdSe–Zn/Ti electrode presented a superior photocurrent response to L-Phe compared to others, which is due to further testifying the formation and modification of molecularly imprinted layer on the electrode surface. The coupling of the low work function marigold follower-like Zn, CdS/CdSe n-n type II heterojunction and bio-moleculgsar imprinting makes a robust strategy for photocurrent increasing. In this electrode, marigold flower-like Zn bonded to the Ti electrode surface and CdS/CdSe can be simultaneously photoexcited, which causes that the L-Phe to be specifically recognized and photo-oxidized on the IPDA layer. Besides, the L-Phe-IPDA-CdS/CdSe–Zn/Ti electrode showed good photocurrent stability for 30 cycles (Fig. 4B).

3.2. Optimization of electron donor

It is a known fact that suitable electron donors and acceptors can convert specific sensing events into corresponding current signals in a typical PEC sensing mechanism. In case of lack of electron donors in the solution to trap holes in this heterojunction systems, the holes will react with S^{2-} and Se^{2-} causing photo-corrosion of CdS and CdSe. Therefore, Na_2S, TEA, and AA as electron donors were selected and revealed the kinds of donors that can increase the photocurrent. The AA was found to be more effective than Na_2S and TEA. Thus, it was selected as an electron donor throughout the experiment.

3.3. Analysis of central composite design

The quadratic model as a significant model was selected and used for operating parameters estimation (Table S2). The regression coefficient values, standard error, and Prob > F value are given in Table S3. It was found that pH (A), applied potential (B), light wavelength (C), their interaction coefficients and their quadratic coefficients were significant at 95%-confidence level since Prob > F of the model was less than 0.001. In fact, the value of Prob > F less than 0.05 indicates that the model term is significant. Therefore, the second-order polynomial effect of the mentioned variables is influential parameters, having the cross-relationship between the PEC responses and studied independent variables as follows:

$$R\ (mA) = +5.21–0.136A + 0.37B-0.41C-0.46AB+0.52AC+0.48BC-0.49A^2+0.044B^2-1.02C^2$$

Two three-dimensional response surfaces were plotted based on the above-mentioned model equation to estimate the PEC biosensor responses over independent variables, as shown in Fig. S1. The plots, given in this figure, reveal the relative effects of two variables on the sensing efficiency. The goodness-of-fit of the regression model would be evaluated regarding the coefficient of determination, R^2 (Fig. S2a) where the regression model had high value (See Table S3). This value indicates that

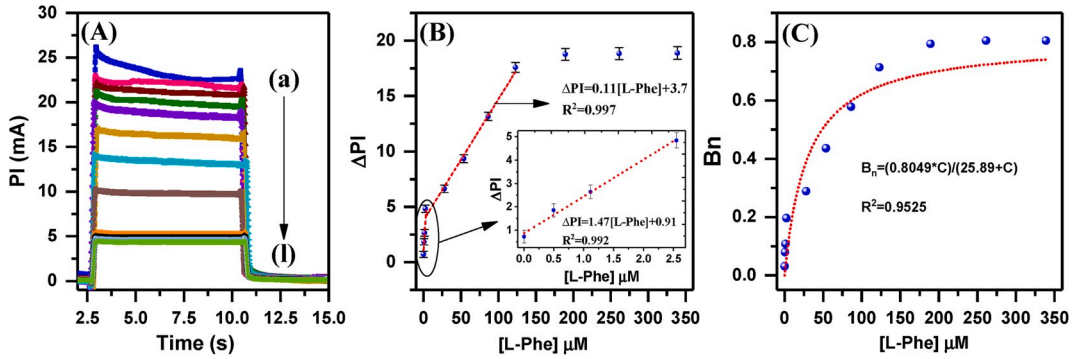

Fig. 5. Effect of different L-Phe concentrations on the photocurrent responses (A), linear calibration curve of (ΔPI) versus various L-Phe concentration (B) (a:0.0 b: 0.005, c: 0.5, d: 1.0, e: 2.5, f: 30; g: 60, h: 90, i: 130, j: 190, K: 260 and l: 340 μM). The calibration curve in top-left inset of (B) is obtained with L-Phe concentration in the range of 0.005–2.5 μM (All points were replicated for 3 time) and binding isotherms of L-Phe to the L-Phe-IPDA-CdS-CdSe-Zn/Ti sensor (C).

94.21% of the variations for the sensing process can be explained by the regression equation, which shows a good agreement between the experimental and predicted values. Leverage, DFFIT and residual values for PEC biosensor responses show no trend and have a small value, confirming the significance of selected model (Fig. S2).

The multi-response optimization desirability function (DF) approach was used as one of the popular and recognized techniques for the determination of optimum setting of input variables and to determine optimum performance levels for one or more responses. Fig. S3 shows the DF profile of the optimal solution for multi-response optimization, in which maximum predicted response value of 5.47 mA for multi-response optimization was obtained at pH 5, 0.6 V applied potential and 540 nm light wavelength.

3.4. Analytical performance of L-Phe-IPDA-CdS/CdSe–Zn/Ti for L-Phe detection

The insulating effect caused by the hindrance effect was directly correlated with L-Phe concentration in two areas (Fig. 5a). The photocurrent signal of as-prepared PEC biosensor without incubating process was denoted as I_0. After incubating in a PBS solution containing 1 mM AA as electron donor, the signal corresponding to different concentrations of L-Phe was represented as I_s. The difference between I_s and I_0 represented as ΔPI was used for the quantification of L-Phe. The I_s decreased and subsequently ΔPI increased with the increase in the concentration of L-Phe over 0.005–2.5 μM due to the enhanced occupation of imprinted pores (fitted line shown in Fig. 5b). After 2.5 μM L-Phe, the I_s decrement was directly related to the L-Phe concentration in a wide linear range from 2.5 to 130 μM with a correlation coefficient of 0.997 (Fig. 5b). The detection limit was calculated to be 0.9 nM based on 3Sb/slope (Sb is the standard deviation of the blank samples). High correlation between the L-Phe concentration and the PI intensity confirmed that in the proposed strategy, more L-Phe target would yield greater hindrance to the mass transport and electron transfer.

In addition, to better understand the result the response signals of the L-Phe-IPDA-CdS-CdSe-Zn/Ti sensor were its normalized, Bn, which calculated according to $B_n = \frac{I_0 - I_S}{I_0}$, and the binding isotherms were generated using B_n values. The values of the dissociation constant (K_D) and the maximum binding response at saturation (B_{max}) were derived from fitting the binding isotherm to Langmuir adsorption model ($B = \frac{CB_{max}}{C+K_D}$). The B_n values were used to plot the binding isotherms (Fig. S4). The L-Phe-IPDA-CdS-CdSe-Zn/Ti sensor showed a hyperbolic response as a function of the L-Phe concentrations. According to the Langmuir adsorption model, when all binding sites are occupied by molecules, no further adsorption will occur on the surface and the saturation response (B_{max}) will be obtained. The fitting results showed that L-Phe-IPDA-CdS-CdSe-Zn/Ti sensor bound the target L-Phe, with the dissociation constant K_D of 25.89 μM.

Table 1
Interferent effect.

Sample	ΔPI_{MIP} (mA)	ΔPI_{NIP} (mA)	IF	R%
L-Phe	7.000	0.106	17.24	100
D-Phe	4.420	0.899	4.92	9.25
Ala	0.590	0.231	2.55	6.56
Gly	0.578	0.220	2.63	5.15
L-cysteine	3.160	0.902	3.50	2.33
Thymine	0.159	0.071	2.23	2.28
Adipic acid	−0.175	0.129	1.35	−2.50
BSA	−0.119	0.094	1.26	−1.70
Guanine	0.103	0.079	1.30	1.47
Adenine	0.140	0.050	2.80	2.00
Tryptophan	0.360	0.103	3.50	2.33
L-Tyr	0.710	0.125	5.69	10.14
D-Tyr	4.023	1.145	3.50	2.33
Citric acid	0.156	0.055	2.83	2.23
Melamine	0.237	0.135	1.75	3.38

The repeatability and reproducibility of the as-prepared PEC sensor was investigated by measuring the PI of 30 μM of L-Phe for 5 times by 5 sensors. The relative standard deviation (RSD%) was as low as 4.0% for entering day and intraday. After 25 days, the PI response remained 92%, which confirmed and validated the outstanding repeatability and stability of the proposed PEC biosensor.

To investigate the selectivity of the as-prepared PEC biosensor towards L-Phe, the effects of common interference was selected as interference conditions on the photocurrent intensity of the L-Phe-IPDA-CdS/CdSe–Zn/Ti and NIPDA-CdS/CdSe–Zn/Ti electrodes (See Table S4). L-Phe-IPDA-CdS/CdSe–Zn/Ti shows negligible change upon immersion into another molecule solution. There is less than 3.0% photocurrent change except for L-Tyr due to the same redox potential of L-Tyr and its chemical structure as well as D-phenylalanine (D-Phe), D-tyrosine (D-Tyr), glycine (Gly) and alanine (Ala) could not easily enter into the L-Phe imprinted cavity, primarily due to shape and functional group mediated diffusional constraints. The imprinting factor (IF), which expresses the ratio of the photocurrent of the target under specific-to-nonspecific binding ($IF = \Delta PI_{MIP}/\Delta PI_{NIP}$) was investigated as an important parameter in evaluating the effectiveness of the imprinting process. The high IF values demonstrate the outstanding selectivity of this bio-PEC sensor, which is mainly due to shape identification, the π-π and electrostatic interaction from IPDA, as well as the higher oxidation ability of L-Phe (See Table 1).

3.5. PEC bioassay mechanism

Organic molecules with proper redox properties can be reduced and/or oxidized by photogenerated electrons and holes, respectively, in a photoelectrochemical platform. Generally, the photogenerated holes

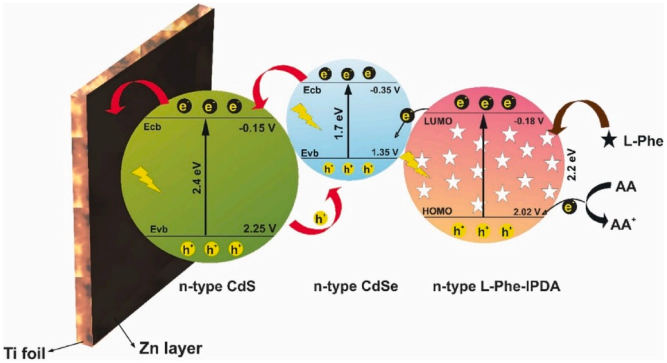

Fig. 6. Possible charge separation diagram and the mechanism of response of L-Phe-IPDA-CdSe/CdS–Zn/Ti heterojunction to L-Phe.

can be reacted with species with lower redox potential on priority and trigger higher photocurrent. Under blue light irradiation, electrons are excited from the occupied VB to the empty CB of CdS, CdSe and L-Phe-IPDA, leaving holes in their VB. The photogenerated electrons in the CB of n-type CdSe transfer to CB of n-type CdS and produce anodic photocurrent while L-Phe-IPDA acts as a selective layer and sensitizing agent (See Fig. 6). Meanwhile, holes are transported in the opposite direction to the heterojunction interface and thus the efficient spatial separation of carriers is achieved. The addition of AA can scavenge photogenerated holes and amplify the anodic photocurrent signal. Besides, after adding L-Phe, it acts as an electron acceptor with steric hindrance effects, which inhibits charge separation, and hence the anodic photocurrent significantly decreases.

3.6. Real sample analysis

The accurate detection of real samples is the ultimate goal of the PEC sensor preparation. Here, standard addition method was applied for real sample detection; before analysis, the urine, apple juice, and grapes juice samples were diluted with PBS. After that, a suitable amount (20, 30 and 40 μM) of the L-Phe solution was injected into all real samples and the parallel L-Phe amount was acquired after the PEC response was tested 3 times. Table S5 lists the results, and it is seen that the RSD is calculated to lower 5% with acceptable recoveries ranging from 65.65 to 104.95%, which provides the evidence of potential possibility in the clinical analysis of L-Phe.

3.7. Comparison with literature

The linear range, limit of detection, transducer type and real sample type were analyzed and compared with other L-Phe sensors reported in the literature (Table S6). As seen, the L-Phe-IPDA-CdS-CdSe-Zn/Ti PEC sensor shows a much better linear range (about three orders of magnitude) and a LOD of 0.9 nM. Moreover, other parameters are satisfactory and comparable to the best L-Phe sensors.

4. Conclusion

In conclusion, a selective PEC biosensor was developed based on a novel strategy by coupling organic photoactive molecular imprinted system with inorganic semiconducting type II heterojunction for PKU monitoring. This strategy proceeds without any enzyme, DNA and bacteria agent where AA was just used as an electron donor label to achieve ultrasensitive and high lifetime photocurrent. In the meantime, this sensitive and selective PEC biosensor minimized the mutual interference. In addition, it was shown to be satisfactorily reproducible, stable, and selective and of acceptable practical application potential. Besides, this work inspires more interests in the design, development, and implementation of various organic and inorganic heterojunctions for advanced MIP-PEC-based bio-analysis in the future.

Declaration of competing interest

There is no conflicted interest.

CRediT authorship contribution statement

Kheibar Dashtian: Conceptualization, Funding acquisition, Writing - original draft. **Shaaker Hajati:** Supervision, Conceptualization, Writing - review & editing. **Mehrorang Ghaedi:** Supervision, Conceptualization, Writing - review & editing.

Acknowledgments

Authors gratefully acknowledge the financial support from the Research Council of the Yasouj University.

Appendix A. Supplementary data

Supplementary data to this article can be found online at https://doi.org/10.1016/j.bios.2020.112346.

References

Aghaei, F., Seifati, S.M., Nasirizadeh, N., 2017. Development of a DNA biosensor for the detection of phenylketonuria based on a screen-printed gold electrode and hematoxylin. Anal. Methods 9 (6), 966–973.
Bang, J.U., Lee, S.J., Jang, J.S., Choi, W., Song, H., 2012. Geometric effect of single or double metal-tipped CdSe nanorods on photocatalytic H2 generation. J. Phys. Chem. Lett. 3 (24), 3781–3785.
Banik, D., Dutta, R., Banerjee, P., Kundu, S., Sarkar, N., 2016. Inhibition of fibrillar assemblies of l-phenylalanine by crown ethers: a potential approach toward phenylketonuria. J. Phys. Chem. B 120 (31), 7662–7670.
Campistol, J., Plecko, B., 2015. Treatable newborn and infant seizures due to inborn errors of metabolism. Epileptic Disord. 17 (3), 229–242.
Cao, J., Ma, Y., Lv, J.-L., Ren, S.-W., Liu, Y.-M., 2020. A potentiometric resolved photoelectrochemical system based on CdS nanowires and SnNb2O6 nanosheets: a case application for dual biomarkers analysis. Chem. Commun. 56, 1513–1516.
Cao, S., Zheng, J., Zhao, J., Wang, L., Gao, F., Wei, G., Zeng, R., Tian, L., Yang, W., 2013. Highly efficient and well-resolved Mn 2+ ion emission in MnS/ZnS/CdS quantum dots. J. Mater. Chem. C 1 (14), 2540–2547.
Chałupniak, A., Merkoçi, A., 2017. Graphene oxide–poly (dimethylsiloxane)-Based lab-on-a-chip platform for heavy-metals preconcentration and electrochemical detection. ACS Appl. Mater. Interfaces 9 (51), 44766–44775.
Charkhabi, S., Beierle, A.M., McDaniel, M.D., Reuel, N.F., 2018. Resonant sensors for low-cost, contact-free measurement of hydrolytic enzyme activity in closed systems. ACS Sens. 3 (8), 1489–1498.
Cheung, K.M., Yang, K.-A., Nakatsuka, N., Zhao, C., Ye, M., Jung, M.E., Yang, H., Weiss, P.S., Stojanović, M.N., Andrews, A.M., 2019. Phenylalanine monitoring via aptamer-field-effect transistor sensors. ACS Sens. 4 (12), 3308–3317.
Christodouleas, D.C., Kaur, B., Chorti, P., 2018. From point-of-care testing to eHealth diagnostic devices (eDiagnostics). ACS Cent. Sci. 4 (12), 1600–1616.
Dashtian, K., Ghaedi, M., Hajati, S., 2019. Photo-Sensitive Pb5S2I6 crystal incorporated polydopamine biointerface coated on nanoporous TiO2 as an efficient signal-on photoelectrochemical bioassay for ultrasensitive detection of Cr (VI) ions. Biosens. Bioelectron. 132, 105–114.
Dashtian, K., Ghaedi, M., Shirinzadeh, H., Hajati, S., Shahbazi, S., 2018. Achieving enhanced blue-light-driven photocatalysis using nanosword-like VO2/CuWO4 type II n–n heterojunction. Chem. Eng. J. 339, 189–203.
Fan, B., Fan, Q., Hu, L., Cui, M., Wang, X., Ma, H., Wei, Q., 2019. Polydopamine-PEG–folic acid conjugate film engineered TiO2 nanotube Arrays for photoelectrochemical sensing of folate binding protein. ACS Appl. Mater. Interfaces 12 (1), 1877–1884.
Hasanzadeh, M., Zargami, A., Baghban, H.N., Mokhtarzadeh, A., Shadjou, N., Mahboob, S., 2018. Aptamer-based assay for monitoring genetic disorder phenylketonuria (PKU). Int. J. Biol. Macromol. 116, 735–743.
Heintz, C., Troxler, H., Martinez, A., Thöny, B., Blau, N., 2012. Quantification of phenylalanine hydroxylase activity by isotope-dilution liquid chromatography–electrospray ionization tandem mass spectrometry. Mol. Genet. Metabol. 105 (4), 559–565.
Hong, Q., Ge, L., Wang, W., Liu, X., Li, F., 2018. Oligonucleotide-modulated photocurrent enhancement of a tetracationic porphyrin for label-free homogeneous photoelectrochemical biosensing. Biosens. Bioelectron. 121, 90–95.
Ibrahim, I., Lim, H.N., Zawawi, R.M., Tajudin, A.A., Ng, Y.H., Guo, H., Huang, N.M., 2018. A review on visible-light induced photoelectrochemical sensors based on CdS nanoparticles. J. Mater. Chem. B 6 (28), 4551–4568.

Idili, A., Parolo, C., Ortega, G., Plaxco, K.W., 2019. Calibration-free measurement of phenylalanine levels in blood using an electrochemical aptamer-based sensor suitable for point-of-care applications. ACS Sens. 4 (12), 3227–3233.
Isabella, V.M., Ha, B.N., Castillo, M.J., Lubkowicz, D.J., Rowe, S.E., Millet, Y.A., Anderson, C.L., Li, N., Fisher, A.B., West, K.A., 2018. Development of a synthetic live bacterial therapeutic for the human metabolic disease phenylketonuria. Nat. Biotechnol. 36 (9), 857–864.
Jafari, M., Rahimi, M.R., Ghaedi, M., Dashtian, K., 2017. ZnO nanoparticles loaded different mesh size of porous activated carbon prepared from Pinus eldarica and its effects on simultaneous removal of dyes: multivariate optimization. Chem. Eng. Res. Des. 125, 408–421.
Khemir, S., El Asmi, M., Sanhaji, H., Feki, M., Jemaa, R., Tebib, N., Dhondt, J.L., Dridi, M.F.B., Mebazaa, A., Kaabachi, N., 2011. Phenylketonuria is still a major cause of mental retardation in Tunisia despite the possibility of treatment. Clin. Neurol. Neurosurg. 113 (9), 727–730.
Kolaei, M., Dashtian, K., Rafiee, Z., Ghaedi, M., 2016. Ultrasonic-assisted magnetic solid phase extraction of morphine in urine samples by new imprinted polymer-supported on MWCNT-Fe3O4-NPs: central composite design optimization. Ultrason. Sonochem. 33, 240–248.
Lee, M.G., Sohn, W., Moon, C.W., Park, H., Lee, S., Jang, H.W., 2016. Conformally coated BiVO4 nanodots on porosity-controlled WO3 nanorods as highly efficient type II heterojunction photoanodes for water oxidation. Nanomater. Energy 28, 250–260.
Long, G., 2013. Integrated design of multifunction TRFIA and phenylketonuria fluorometer. Laser Optoelectr. Prog. (5), 16.
Lv, S., Zhang, K., Zeng, Y., Tang, D., 2018. Double photosystems-based 'Z-Scheme'photoelectrochemical sensing mode for ultrasensitive detection of disease biomarker accompanying three-dimensional DNA walker. Anal. Chem. 90 (11), 7086–7093.
MacDonald, A., Lilburn, M., Cochrane, B., Davies, P., Daly, A., Asplin, D., Hall, S., Cousins, A., Chakrapani, A., Robinson, P., 2004. A new, low-volume protein substitute for teenagers and adults with phenylketonuria. J. Inherit. Metab. Dis. 27 (2), 127–135.
Mao, L., Wang, X., Guo, Y., Yao, L., Xue, X., Wang, H.-X., Xiong, C., Wen, W., Zhang, X., Wang, S., 2019. A synergistic approach to enhance the photoelectrochemical performance of carbon dots for molecular imprinting sensors. Nanoscale 11 (16), 7885–7892.
Min, J., Nothing, M., Coble, B., Zheng, H., Park, J., Im, H., Weber, G.F., Castro, C.M., Swirski, F.K., Weissleder, R., 2018. Integrated biosensor for rapid and point-of-care sepsis diagnosis. ACS Nano 12 (4), 3378–3384.
Moreira, C.M., Pereira, S.V., Raba, J., Bertolino, F.A., Messina, G.A., 2018. Based enzymatic platform coupled to screen printed graphene-modified electrode for the fast neonatal screening of phenylketonuria. Clin. Chim. Acta 486, 59–65.
Naghib, S.M., Rabiee, M., Omidinia, E., Khoshkenar, P., 2012. Investigation of a biosensor based on phenylalanine dehydrogenase immobilized on a polymer-blend film for phenylketonuria diagnosis. Electroanalysis 24 (2), 407–417.
Qiu, Z., Shu, J., Tang, D., 2018. Near-infrared-to-ultraviolet light-mediated photoelectrochemical aptasensing platform for cancer biomarker based on core–shell NaYF4: Yb, Tm@ TiO2 upconversion microrods. Anal. Chem. 90 (1), 1021–1028.
Sassolas, A., Blum, L.J., Leca-Bouvier, B.D., 2012. Immobilization strategies to develop enzymatic biosensors. Biotechnol. Adv. 30 (3), 489–511.
Shi, H., Wang, Y., Tang, C., Wang, W., Liu, M., Zhao, G., 2019a. Mechanisim investigation on the enhanced and selective photoelectrochemical oxidation of atrazine on molecular imprinted mesoporous TiO2. Appl. Catal. B Environ. 246, 50–60.
Shi, L., Yin, Y., Zhang, L.-C., Wang, S., Sillanpää, M., Sun, H., 2019b. Design and engineering heterojunctions for the photoelectrochemical monitoring of environmental pollutants: a review. Appl. Catal. B Environ.
Shou, W., Mahajan, B.K., Ludwig, B., Yu, X., Staggs, J., Huang, X., Pan, H., 2017. Low-cost manufacturing of bioresorbable conductors by evaporation–condensation-mediated laser printing and sintering of Zn nanoparticles. Adv. Mater. 29 (26), 1700172.
Song, Z., Fan, G.-C., Li, Z., Gao, F., Luo, X., 2018. Universal design of selectivity-enhanced photoelectrochemical enzyme sensor: integrating photoanode with biocathode. Anal. Chem. 90 (18), 10681–10687.
Szabó, E., Szatmári, I., Szőnyi, L.s., Takáts, Z.n., 2015. Quantitative analytical method for the determination of biotinidase activity in dried blood spot samples. Anal. Chem. 87 (20), 10573–10578.
Tabatabaei, N., Dashtian, K., Ghaedi, M., Sabzehmeidani, M.M., Ameri, E., 2018. Novel visible light-driven Cu-based MOFs/Ag 2 O composite photocatalysts with enhanced photocatalytic activity toward the degradation of orange G: their photocatalytic mechanism and optimization study. New J. Chem. 42 (12), 9720–9734.
Tiwari, J.N., Vij, V., Kemp, K.C., Kim, K.S., 2016. Engineered carbon-nanomaterial-based electrochemical sensors for biomolecules. ACS Nano 10 (1), 46–80.
Tsafack, V.C., Marquette, C.A., Leca, B., Blum, L.J., 2000. An electrochemiluminescence-based fibre optic biosensor for choline flow injection analysis. Analyst 125 (1), 151–155.
Wang, C., Ye, X., Wang, Z., Wu, T., Wang, Y., Li, C., 2017a. Molecularly imprinted photoelectrochemical sensor for human epididymis protein 4 based on polymerized ionic liquid hydrogel and gold nanoparticle/ZnCdHgSe quantum dots composite film. Anal. Chem. 89 (22), 12391–12398.
Wang, R., Ma, H., Zhang, Y., Wang, Q., Yang, Z., Du, B., Wu, D., Wei, Q., 2017b. Photoelectrochemical sensitive detection of insulin based on CdS/polydopamine co-sensitized WO3 nanorod and signal amplification of carbon nanotubes@ polydopamine. Biosens. Bioelectron. 96, 345–350.
Wick, S., Walsh III, D.I., Bobrow, J., Hamad-Schifferli, K., Kong, D.S., Thorsen, T., Mroszczyk, K., Carr, P.A., 2019. PERSIA for direct fluorescence measurements of transcription, translation, and enzyme activity in cell-free systems. ACS Synth. Biol. 8 (5), 1010–1025.
Wongkaew, N., Simsek, M., Griesche, C., Baeumner, A.J., 2018. Functional nanomaterials and nanostructures enhancing electrochemical biosensors and lab-on-a-chip performances: recent progress, applications, and future perspective. Chem. Rev. 119 (1), 120–194.
Xu, K., 2019. Silicon MOS optoelectronic micro-nano structure based on reverse-biased PN junction. Phys. Status Solidi 216 (7), 1800868.
Xu, K., Chen, Y., Okhai, T.A., Snyman, L.W., 2019a. Micro optical sensors based on avalanching silicon light-emitting devices monolithically integrated on chips. Opt. Mater. Express 9 (10), 3985–3997.
Xu, X., Ji, D., Zhang, Y., Gao, X., Xu, P., Li, X., Liu, C.-C., Wen, W., 2019b. Detection of phenylketonuria markers using a ZIF-67 encapsulated PtPd alloy nanoparticle (PtPd@ ZIF-67)-based disposable electrochemical microsensor. ACS Appl. Mater. Interfaces 11 (23), 20734–20742.
Yan, Y., Jin, X., Wang, X., Zhang, C., Zhang, Q., Zheng, L., Feng, X., Hao, S., Gao, H., Ma, X., 2020. Screening of PAH common mutations in Chinese phenylketonuria patients using iPLEX MALDI-TOF MS. ACS Omega 5 (4), 1805–1812.
Yang, W., Hu, K., Teng, F., Weng, J., Zhang, Y., Fang, X., 2018. High-performance silicon-compatible large-area UV-to-visible broadband photodetector based on integrated lattice-matched type II Se/n-Si heterojunctions. Nano Lett. 18 (8), 4697–4703.
Yang, X., Gao, Y., Ji, Z., Zhu, L.-B., Yang, C., Zhao, Y., Shu, Y., Jin, D., Xu, Q., Zhao, W.-W., 2019. Dual functional molecular imprinted polymer-modified organometal lead halide perovskite: synthesis and application for photoelectrochemical sensing of salicylic acid. Anal. Chem. 91 (15), 9356–9360.
Yu, Y., Huang, Z., Zhou, Y., Zhang, L., Liu, A., Chen, W., Lin, J., Peng, H., 2019. Facile and highly sensitive photoelectrochemical biosensing platform based on hierarchical architectured polydopamine/tungsten oxide nanocomposite film. Biosens. Bioelectron. 126, 1–6.
Zhao, W.-W., Xu, J.-J., Chen, H.-Y., 2017. Photoelectrochemical enzymatic biosensors. Biosens. Bioelectron. 92, 294–304.
Zhou, L., Hu, Q., Kang, Q., Fang, M., Yu, L., 2018. Construction of a liquid crystal-based sensing platform for sensitive and selective detection of L-phenylalanine based on alkaline phosphatase. Langmuir 35 (2), 461–467.